Optical Sensor with Wide Range and High Sensitivity for Internal Magnetic Field Detection of Transformer

Meng Huang, *Member*, *IEEE*, *Member*, *CSEE*, Wei Zheng, Tong Ji, Mao Ji, Tianjiao Pu, *Senior Member*, *IEEE*, *Fellow*, *CSEE*, and Bo Qi, *Senior Member*, *IEEE*, *Senior Member*, *CSEE*

***Abstract*—The deterioration of winding defects is one of the important causes of power transformer fires and even explosion failures. The change of leakage magnetic field distribution is the most direct response to winding defects. Currently there are few sensors suitable for online measurement of the internal magnetic field of transformers. Based on the Faraday magneto-optical effect, a magnetic field sensor with wide range and high sensitivity is proposed in this paper, which is suitable for the interior use of transformers. The straight-through optical structure with interior polarizer is adopted, and the sensor has a measurement range of 1.5 T and a sensitivity of 1 mT. It also possesses a small size, with a length of about 30 mm after encapsulation. The influence mechanism of vibration and temperature is revealed through theoretical analysis and numerical simulation. It is proposed to filter out the interference of vibration by characteristic frequency analysis and to compensate for temperature by a two-probe structure. An anti-interference test verifies the effectiveness of this method, and it can reduce the error from 80.56% to 2.63% under the combined interference of vibration and temperature.**

***Index Terms*—Anti-interference, Bessel function, Faraday magneto-optical effect, leakage magnetic field, transformer, two-probe structure.**

I. Introduction

POWER transformer is the key equipment in the power system, so it's safe and stable operation directly affects the reliability of the power system. Transformer winding defects such as winding deformation and inter-turn short circuit, are one of the main causes of transformer accidents. If the transformer continues to operate after winding defects occur, it will gradually develop into a through long-distance arc fault [1], [2]. When a large-energy arc discharge occurs in the enclosed space of a power transformer, a huge shock pressure wave will be generated, which can easily cause the transformer box to rupture, explode and catch fire [3], and sometimes even directly threaten the life safety of on-site staff. Therefore, timely and effective monitoring of transformer winding defects can ensure the safe and stable operation of the transformer, thereby improving the reliability of the power system [4], [5].

When winding deformation or inter-turn short circuit occurs to a transformer, it directly changes the distribution of the leakage magnetic field inside the transformer [2], [6]. Therefore, monitoring the transformer leakage magnetic field provides a new idea for online monitoring of the above two typical kinds of winding defects. Due to the shielding effect of the transformer metal box and the magnetic shielding design of power transformer, it is difficult to measure the leakage magnetic field outside, so it needs to be measured inside the transformer, but there is a lack of effective transformer built-in magnetic field sensors (MFS).

Optical MFSs have a bright future in transformer leakage magnetic field monitoring due to their advantages of anti-electromagnetic interference. There are three kinds of optical MFSs based on fiber grating, fiber interferometer, and Faraday Effect, respectively. The fiber grating needs to be combined with magnetostrictive material, but the fiber grating is susceptible to acoustic signals, vibration, temperature, pressure, etc. Measurement range is mainly within 0.1 T [7], while the leakage magnetic field during an inter-turn short circuit fault can reach about 1.5 T [2], [6]. The optical fiber interference one also needs to be combined with the magnetostrictive material, and the interferometric fiber optical MFS usually has high sensitivity [8]. Reference [9] has designed an MFS with a resolution of 4.59 nT, but the measurement range is less than 0.14 mT, which is much lower than the measurement requirement for transformer leakage magnetic field. Sensor's size is a little large, which is about 80 mm in length, and the magnetostrictive material used as the sensitive element is a conductor, which is not suitable for the installation inside a transformer. The sensing material of the sensor based on the Faraday Effect can be either a magneto-optical crystal (MOC) or a sensing optical fiber [10], [11]. The measuring range of the sensor can reach 3.2 T [10], which meets the variation range of the leakage magnetic field in transformer. The Verdet constant of the all-fiber MFS is smaller than MOC, and the linear birefringence is larger. Relatively speaking, the MOC MFS is simple in structure, small in size, light in weight, and

Manuscript received October 24, 2022; revised January 2, 2023; accepted February 8, 2023. Date of online publication February 14, 2024; date of current version March 20, 2024. This work was supported in part by the National Key R&D Program of China (No. 2020YFB0905902).

M. Huang (corresponding author, email: hm2016@ncepu.edu.cn), W. Zheng, T. Ji, M. Ji, and B. Qi are with the State Key Laboratory of Alternate Electrical Power System with Renewable Energy Sources, North China Electric Power University, Beijing 102206, China.

M. Huang and B. Qi are also with the Beijing Key Laboratory of High Voltage & EMC, North China Electric Power University, Beijing 102206, China.

T. J. Pu is with China Electric Power Research Institute, Beijing 100192, China.

DOI: 10.17775/CSEEJPES.2022.07270

2096-0042 © 2022 CSEE. This is an open access article under the CC BY-NC-ND license (http://creativecommons.org/licenses/by-nc-nd/4.0/).

high in stability, so it is more suitable for on-line measurement of transformer leakage magnetic field.

The Faraday magneto-optical effect is often used in the optical measurement of magnetic fields and currents, and current transformers attract most attention, at present. However, current measurement makes use of the magnetic field induced by the current, so its essence is still magnetic field measurement. Numerous studies have shown that temperature and stress are the two key factors for the Faraday magneto-optical effect [12]. An MFS with a sensitivity of 8 nT is obtained by using a YIG ($Y_3Fe_5O_{12}$) MOC with a high Verdet constant, but it is difficult to overcome the influence of temperature on the stability [10]. During the operation of transformer, the winding and the tank wall will vibrate, and the temperature inside the transformer will also change with the operating conditions. They will change the deflection angle of light in the optical fiber and MOC, which will affect the measurement accuracy of the optical MFS. The leakage magnetic field of a normal transformer is weak, and the change of the leakage magnetic field is in the level of mT when winding deformation takes place, while it can reach about 1.5 T when the inter-turn short circuit occurs [2], [6]. However, there is rare literature on the optical MFS for detecting transformer leakage magnetic field at present. An MFS based on terbium gallium garnet (TGG) crystal with the measurement range of -6 T$\sim$6 T has been proposed, but the resolution is just about 10 mT [13]. Though an MFS with a higher resolution of 0.224 mT is realized, the operating range is merely 200 mT [14]. Moreover, neither of them have considered the influence of vibration nor temperature. Therefore, it is necessary to develop an MFS with good insulation performance, wide range and high sensitivity, and being resistant to temperature and vibration interference.

Based on the Faraday Effect, this paper proposes a wide-range and high-sensitivity MFS suitable for measurement of the leakage magnetic field inside a power transformer. The second section introduces the sensing principle of the magnetic field, the design of the optical structure, and the analysis of the interference mechanism of vibration and temperature. On this basis, we propose the characteristic frequency analysis method to suppress the interference of vibration and adopt the two-probe structure to compensate for the interference of temperature. The third part describes the structure design of the sensor, and theoretically analyzes the working principle, measurement accuracy, anti-interference ability and sensitivity of the sensor through simulation. In the fourth part, the effectiveness of the anti-interference method is verified by the interference test, and the accuracy, sensitivity and measurement range of the sensor are verified by the performance calibration test. The conclusion summarizes the principle and performance of the sensor, and analyzes the current shortcomings and future improvement directions.

II. Sensing Principle

A. Principle of Magnetic Field Sensing

The main component of an MFS based on the Faraday effect is the sensing probe containing an MOC. Under the action of a magnetic field, when the incident linearly polarized light (LPL) passes through the MOC in the probe, the polarization plane of the LPL rotates by θ, and its relationship with the magnetic field is [10], [11]:

$$\theta = BVL \tag{1}$$

where V is the Verdet constant of the MOC, L is the length of the MOC, and B is the amplitude of the magnetic field.

By measuring the change of light intensity, the Faraday rotation angle is obtained indirectly, and hence the magnetic field measurement is realized. The angle between the polarization directions of the two polarizers is 45°, so the output light intensity P is only related to the initial output light intensity I and the Faraday rotation angle. Once the Verdet constant and length of the MOC are known, and so is the initial output light intensity, the magnetic field strength can be obtained by measuring the output light intensity [13]:

$$P = \frac{1}{2}I \cdot [1 + \sin 2\theta] = \frac{1}{2}I \cdot [1 + \sin 2(BVL)] \tag{2}$$

Research shows that the leakage magnetic field inside a transformer is 10–300 mT [13], [15], and the variation of the leakage magnetic field is about several mT when the winding deformation is slight [15], [16]. Although the probe size of straight-through optical structure with interior polarizer is slightly larger, it has obvious advantages in highly sensitive measurement of a weak magnetic field, so it is chosen for the sensor, as shown in Fig. 1.

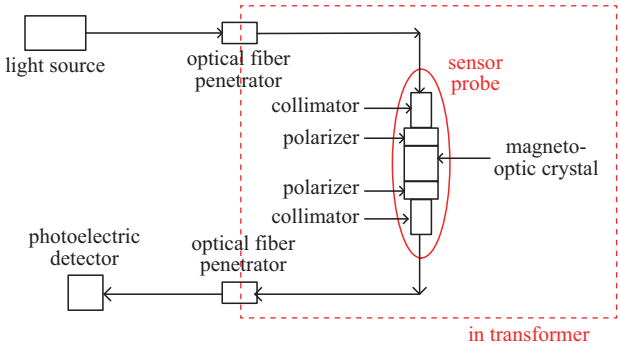

Fig. 1. Straight-through optical structure with interior polarizer for measuring magnetic field based on Faraday Effect.

The frequency of the leakage magnetic field is 50 Hz for a transformer with a rated frequency of 50 Hz. From (2), it can be known the change of the output light intensity of the probe caused by the magnetic field can be expressed as:

$$P = \frac{I}{2}\{1 + \sin[2VLB\cos(\omega_0 t)]\} \tag{3}$$

where t is time, ω_0 is the angular frequency of the magnetic field, and its value is 314.16 rad/s. To ensure both a wide range and high sensitivity in magnetic field measurement, the deflection angle of the MOC should be less than $\pi/8$ (which will be discussed later), so the second term on the right side of (3) can be simplified by using the characteristics of the first kind Bessel function and omitting higher-order terms [17], then (3) becomes

$$P = \frac{I}{2}[1 + A_3\cos(\omega_0 t)] \tag{4}$$

where A_3 is a coefficient related to the deflection angle of the MOC, and it is less than one. It can be seen that the amplitude of the magnetic field at the probe can be obtained from the amplitude of the 50 Hz component in its output light intensity spectrum.

B. Interference Mechanism and Suppression Method of Vibration

Since the intrinsic circular birefringence of the fiber is very small, this influence can be ignored [17], [18], but the vibration will induce bending and stressing on the fiber, thus causing the change of the linear birefringence of the fiber [17]. The phase difference $\Delta\phi$ between the two orthogonal polarization axes of the linear birefringence caused by the vibration can be represented as [19]:

$$\Delta\phi = a\cos(\omega t + \theta) \tag{5}$$

where a is a constant, related to the amplitude of the vibration, the length of the disturbed fiber, and the intrinsic parameters of the fiber, such as fiber radius, photo-elastic coefficient, and refraction index, and ω and θ are the frequency and initial phase of the vibration, respectively.

Assuming that the initial phase difference of the two polarization axes is ϕ, and the angle between the LPL from the light source and the first polarizer in Fig. 1 is δ, the light intensity P_{M} entering the MOC can be expressed as:

$$P_{\mathrm{M}} = I \cdot [1 - \sin(2\delta)\cos(\phi + a\cos(\omega t + \theta))] \tag{6}$$

Because the vibration amplitude of transformer is usually weak, (6) can be simplified to (7) using the Bessel function and omitting the high-order terms, too [17]:

$$P_{\mathrm{M}} = I \cdot [A_0 + A_1\cos(\omega t + \theta)] \tag{7}$$

where A_0 is a constant related to ϕ and δ, and A_1 is a coefficient related to the vibration amplitude. We can see that the spectrum of the light intensity entering the MOC contains a direct current (DC) component and an alternating component, which is related to the amplitude of the vibration and has the same frequency as the vibration.

The length of the MOC in the probe is much smaller than of the optical fiber and its diameter is much larger than of the optical fiber, therefore the deformation of the MOC caused by the vibration is small. The birefringence of the MOC is smaller than of the optical fiber too, so the influence of the vibration on the deflection angle of the MOC can be ignored. From (4) and (7), the output light intensity of the probe caused by the magnetic field and vibration can be expressed as:

$$P = \frac{I}{2} \cdot [A_0 + A_1\cos(\omega t + \theta)][1 + A_3\cos(\omega_0 t)] \tag{8}$$

Equation (8) is further expanded to obtain (9), and its fourth term means that two cross components with equal amplitudes and frequencies of ω-ω_0 and $\omega + \omega_0$ will be generated.

$$\begin{aligned} P = \frac{I}{2} \cdot [&A_0 + A_1\cos(\omega t + \theta) + A_0 A_3\cos(\omega_0 t) \\ &+ A_1 A_3\cos(\omega t + \theta)\cos(\omega_0 t)] \end{aligned} \tag{9}$$

The vibration frequencies of the transformer with a rated frequency of 50 Hz are integer multiples of 100 Hz [20], but the frequency of the leakage magnetic field in the transformer is 50 Hz. So, the frequency corresponding to ω is an integer multiple of 100 Hz, the frequency corresponding to ω_0 is 50 Hz, and the frequencies corresponding to $\omega - \omega_0$ and $\omega + \omega_0$ are odd multiples of 50 Hz. Once there is a vibration of 100 Hz, the $\omega - \omega_0$ component will contain a 50 Hz interference signal. This influence of the cross component on the magnetic field measurement needs to be considered. By taking advantage of the feature that the amplitudes of the $\omega - \omega_0$ and $\omega + \omega_0$ components are equal, we can subtract a component with amplitude being equal to the $\omega + \omega_0$ component from the $\omega - \omega_0$ one of the output light intensity.

According to (9), after eliminating the interference of the cross component, the ratio of the two characteristic frequency components of 50 Hz and DC in the output light intensity is equal to A_3, from which the deflection angle of the MOC in the probe can be obtained, thereby suppressing the interference of the vibration and obtaining the magnetic field strength at the probe.

C. Interference Mechanism and Compensation Method of Temperature

From (1), we can see the deflection angle of the LPL after passing through the MOC is related to not only the magnetic field strength but also the Verdet constant of the MOC. The Verdet constant usually changes with temperature, for example, the Verdet constant of TGG crystal is temperature dependent, and as the temperature increases, the Verdet constant decreases, when the wavelength of the light source is fixed [21]. Generally speaking, within a certain temperature range, Verdet constant ratios of MOCs with different Verdet constants are unique at different temperatures, as shown in Fig. 2(a). Therefore, a two-probe structure can be used to compensate for temperature interference [22]. The two probes are composed of two kinds of MOCs with different Verdet constants, as shown in Fig. 2(b). When the two probes are in the same spatial position (that is, the ambient temperature and magnetic field are identical), the Faraday rotation angle is different due just to the difference of the Verdet constant. If they are marked as θ_1 and θ_2, respectively, the Faraday rotation angles of the two probes satisfy the relationship illustrated in (10):

$$f(T) = \frac{V_1(T)}{V_2(T)} = \frac{\theta_1}{\theta_2} \tag{10}$$

where $V_1(T)$ and $V_2(T)$ are the Verdet constants of the MOCs in the two probes, respectively, $f(T)$ is the ratio function of the Verdet constants of the MOCs in the two probes at different temperatures.

Since $f(T)$ can be obtained by calibration in advance, the temperature can be obtained from (10) according to the Faraday rotation angle of the two probes. The change of the internal temperature of transformer is usually slow, so the change of the temperature at the moment of data acquisition can be ignored, and it can be seen that V in (3) does not change with time. Therefore, according to the relationship between the

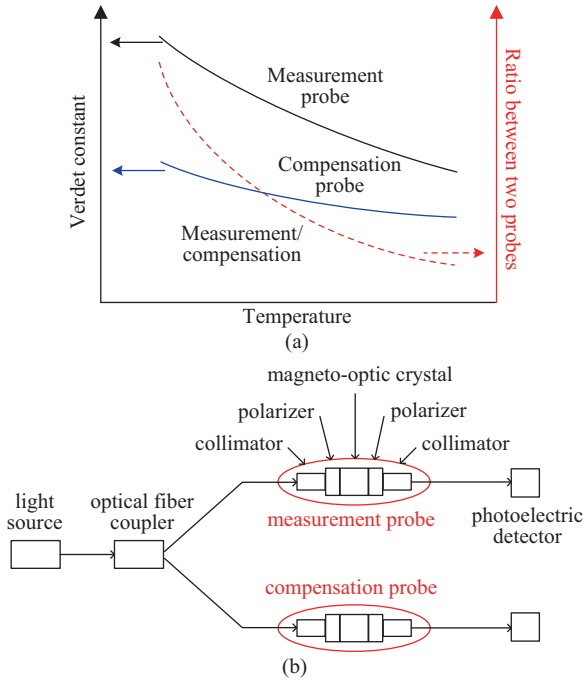

Fig. 2. Schematic diagram and structure of the two-probe sensor. (a) Schematic diagram of the ratio of Verdet constants of the two-probe sensor. (b) Sensor structure based on the two-probe topology.

coefficient A_3 and the deflection angle θ in (3) and (4), we can obtain the Faraday rotation angle and temperature from the 50 Hz component of the output light intensity of the two probes. Then with one of the probes (named as measurement probe) after temperature calculation, the magnetic field can be obtained from the Faraday rotation angle and temperature compensated Verdet constant.

D. Treatment of Vibration and Temperature Combined Interference

From the above, the vibration interference is mainly coupled in through the optical fiber between the light source and the probe, while the temperature interference is mainly coupled in through the MOCs in the probes. Therefore, vibration has no effect on the working principle of the two-probe structure. Equations (8) to (9) are applicable to both measurement and compensation probes. The coefficient A_3 of each probe can be obtained by using the suppression method for vibration interference in Section II-B. Then, according to the compensation method for temperature interference in Section II-C, the strength of the magnetic field at the position of the probe can be obtained, so as to realize the anti-interference under the vibration and temperature combined interference.

III. Sensor Fabrication and Theoretical Analysis

A. Probe Structure of the Sensor

According to Section II-A, the Verdet constant of the MOC determines the sensitivity and range of the magnetic field measurement. Meanwhile, the difference between the Verdet constants of the two MOCs should not be too large, and their ratio function $f(T)$ at different temperatures should have an invertible function. MOCs should possess a high saturation magnetic field, as the leakage magnetic field can reach 1.5 T once the inter-turn short circuit occurs [6]. The saturation magnetic field of TGG and Terbium Scandium Aluminum Garnet (TSAG) crystal is greater than 3 T, and the Verdet constants at 1310 nm are about 20.7 rad/(T·m) and 27.9 rad/(T·m), respectively [23]. It can ensure that the probe is small in volume and has wide dynamic measurement range and high sensitivity. Besides, the performance of the two crystals is similar, making them suitable for composing a two-probe structure.

The wavelength of the light source used is 1310 nm, the output light intensity is adjustable from 0 to 50 mW, and it fluctuates less than 0.2% within 24 hours. The measured variation curves of the Verdet constants of TGG and TSAG crystals are shown in Fig. 3. It can be seen with the increase of temperature, the Verdet constants of both crystals decrease. Fig. 3 also shows the ratio of the Verdet constants of TSAG and TGG crystals at different temperatures. In the range of 25 to 95°C, with the increase of temperature, the ratio function $f(T)$ decreases monotonically, indicating $f(T)$ is reversible, so that the temperature can be obtained according to the ratio of the deflection angles of the two crystals.

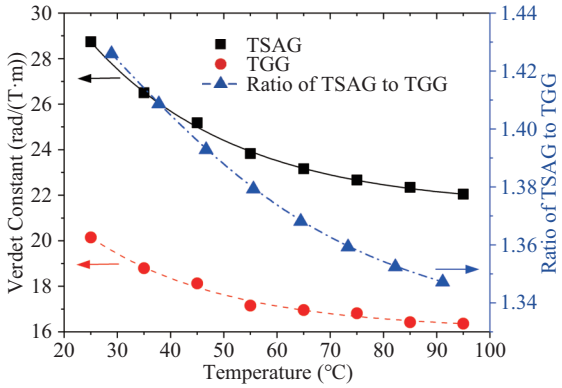

Fig. 3. Temperature dependent Verdet constants of TSAG and TGG.

According to (1), after the Verdet constant is determined, the maximum measurable magnetic field depends on the maximum measurable Faraday rotation angle and the length of the MOC. Because the straight-through optical structure with the angle between the polarizer and the analyzer is 45°, when the Faraday rotation angle is 0°, the sensitivity is the largest. The maximum measurable Faraday rotation angle is theoretically 45°, but when it is close to 45°, the sensitivity of the sensor decreases, which is not beneficial to the measurement of the leakage magnetic field [13], so the maximum Faraday rotation angle is taken as 20°, which can not only ensure the sensor has a wide measurement range and high sensitivity, but also can eliminate the influence of higher-order terms when measuring AC magnetic field. When the TSAG crystal is selected as the measurement probe, and the crystal length is 8 mm, it can meet the requirement of the maximum measurable magnetic field of about 1.5 T.

With the help of a five-dimensional optical translation platform, the collimator, polarizer, and MOC were added to the

rigid support in turn, and the angle between the two polarizers was adjusted to 45°, and then bonded and fixed by adding optical glue. The final size of the single probe of the sensor is 8 mm in outer diameter and 30 mm long, as shown in Fig. 4.

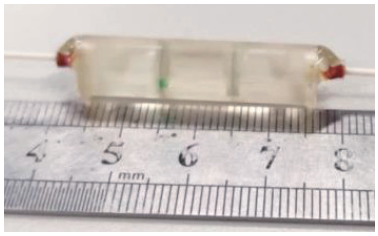

Fig. 4. Image of a single probe of the sensor.

B. Light Intensity Simulation under Different Conditions

Using (3), (5), (6), and (9), we calculate the output light intensity of the sensor under different conditions with numerical calculation software.

1) Under No-interference Conditions

The length of the MOC is taken as the actual length of 8 mm, and the Verdet constant of the MOC is taken as the measurement result of TSAG at 25°C from Fig. 3. The time-domain and frequency-domain waveforms of the output light intensity under a mere 50 Hz alternating magnetic field are shown in Fig. 5. It can be seen that the time-domain waveform output light intensity alternates with the main frequency of 50 Hz, and the greater the magnetic field strength, the greater the variation of the output light intensity. As regards the frequency-domain waveform, the DC component remains unchanged under different magnetic fields, while the amplitude of the 50 Hz component increases with the increase of the magnetic field strength. In addition, there is a small amount of 150 Hz component, but the amplitude is very small, less than 5% of the 50 Hz component, which can be ignored [24]. This is consistent with the previous theoretical analysis and assumptions.

According to (4), the amplitude of the 50 Hz component normalized to the DC component is exactly the coefficient A_3. Fig. 5(c) shows the relationship between the coefficient A_3 of the light intensity fluctuation and the magnetic field strength. It can be seen the value of A_3 is less than one, and has good linear relationship with the peak value of the magnetic field strength, where the linear accuracy of fit is 0.9997.

2) Influence of Vibration Interference

To analyze the influence of vibration on the measurement results of the magnetic field, the influence of vibration on the light intensity entering the MOC is first simulated. From (5) and (6), it can be deduced that the initial phase θ of the vibration has an influence on the time domain waveform of the light intensity. However, it has no effect on the frequency domain analysis, so the effect of θ can be ignored and zero is taken in the simulation. The variation amplitude a of the fiber birefringence deflection angle caused by vibration is usually much less than 1 rad [17], which is taken as $\pi/6$ in the simulation. The angle δ between the output LPL from the light source and the first polarizer can be any value, but according

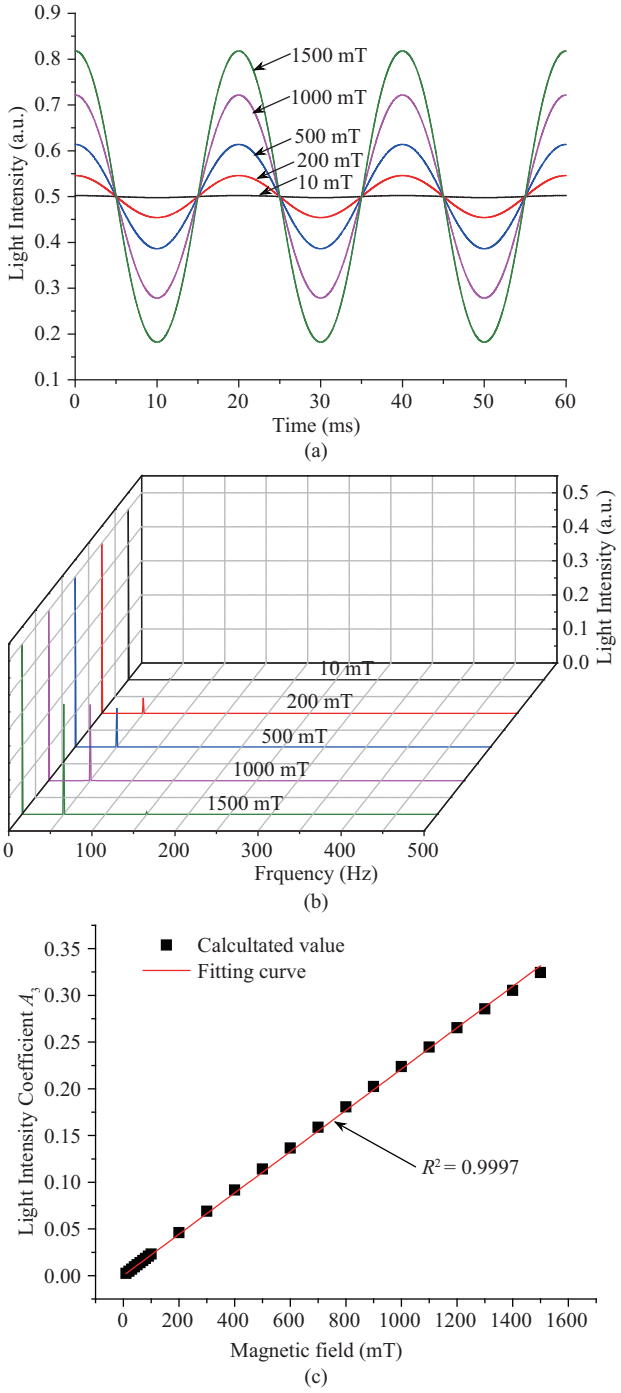

Fig. 5. Variation of output light intensity under different magnetic fields. (a) Time domain waveform. (b) Frequency domain waveform. (c) Relationship between A3 and magnetic field.

to the periodicity and symmetry of the value of $\sin(2\delta)$, only the situation when it is $0 \sim \pi/4$ should be considered. The initial phase difference ϕ of the two polarization axes is usually very small [18]. Fig. 6 shows the simulation results when δ is $0 \sim /4\pi$ and ϕ is $0 \sim \pi/6$, and the vibration frequency is 100 Hz [20]. Within the given range, the larger the values of δ and ϕ are, the greater the change in the light intensity caused by the vibration. The frequency domain results in Fig. 6 show that no matter how the time domain light intensity waveform changes, it is mainly composed of DC component,

100 Hz component and a small amount of 200 Hz component, and the other higher frequency components can be ignored, which is consistent with the previous theoretical analysis and assumptions. Therefore, take $\delta = \pi/4$ and $\phi = \pi/6$ to simulate and analyze the impact of vibration next.

The changes of light intensity caused by vibration and different magnetic fields are shown in Fig. 7(a). It can be seen that the positions of the peaks and troughs of light intensity changes are consistent with those in Fig. 6(a), but the amplitudes of the adjacent two peaks are not equal any more. The magnetic field increases the amplitude of one peak while decreases the other one. This is because the deflection angle of the MOC is alternately changed caused by the 50 Hz alternating magnetic field, making its peak value changes every 10 ms. The larger the magnetic field, the greater the difference between adjacent two peaks. But no matter what the amplitude of the magnetic field is, the values of the troughs of light intensity do not change.

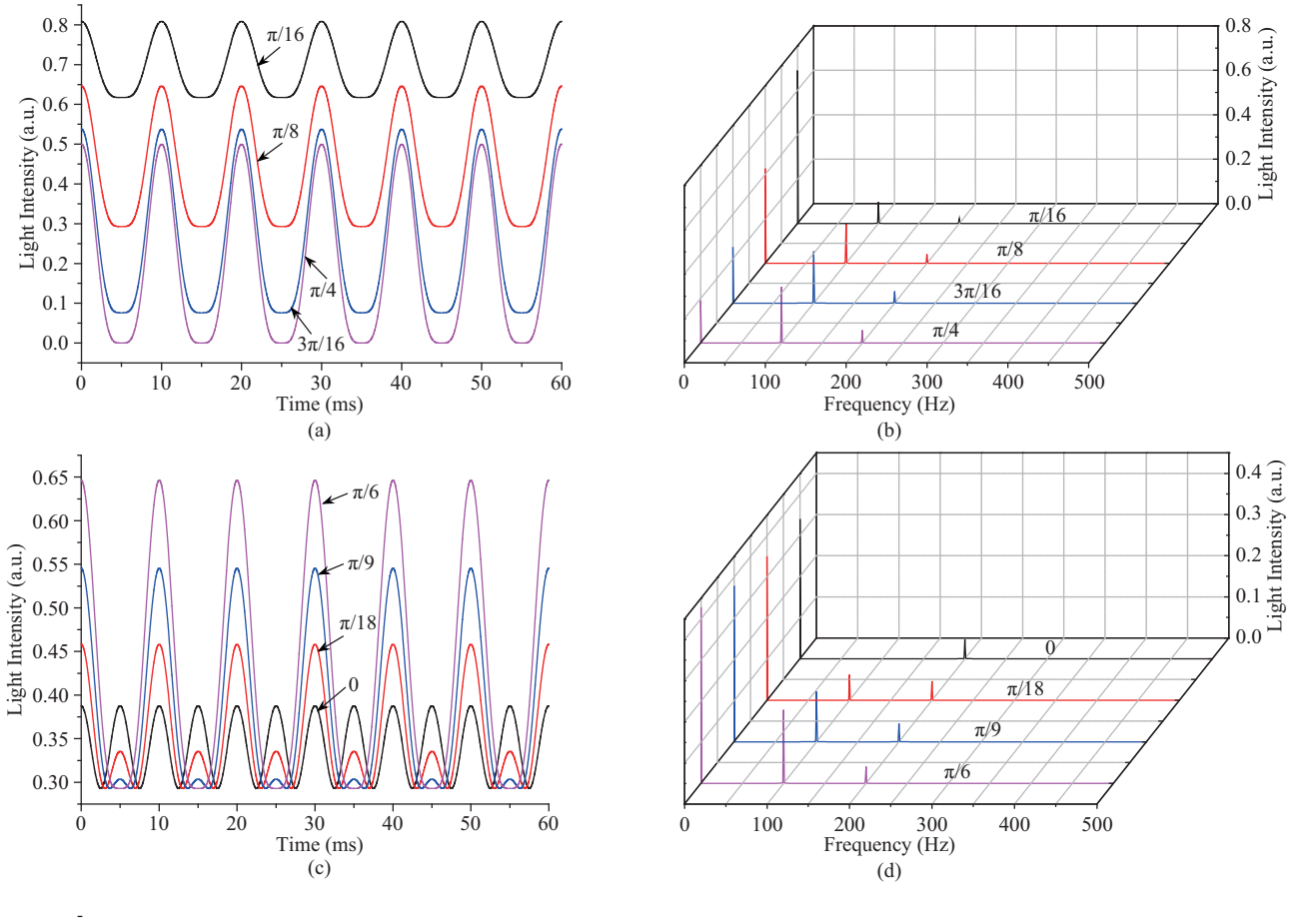

Fig. 6. Influence of δ and ϕ on incident light intensity of the MOC. (a) Influence of δ on time domain waveform. (b) Influence of δ on frequency domain waveform. (c) Influence of ϕ on time domain waveform. (d) Influence of ϕ on frequency domain waveform.

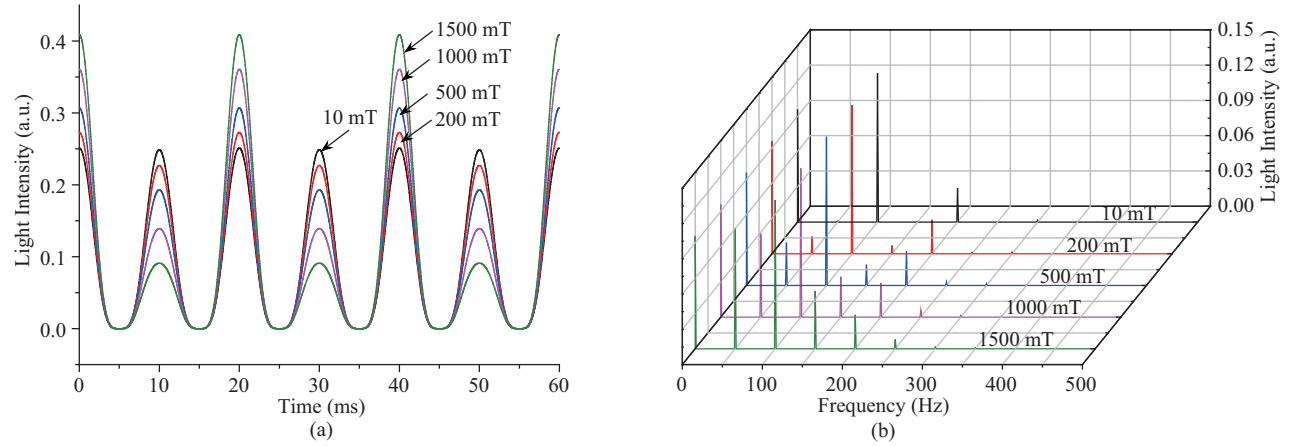

Fig. 7. Variation of light intensity under vibration and different magnetic fields. (a) Time domain waveform. (b) Frequency domain waveform.

Figure 7(b) is the frequency-domain waveform corresponding to Fig. 7(a). Except for the DC component, components of 50 Hz and 150 Hz clearly appear in Fig. 7(b), which is consistent with the theoretical analysis. Using the previous cross component analysis and interference separation method, the DC component P_0 and 50 Hz component P_{50} of the output light intensity under different magnetic fields are obtained, as shown in Table I. With the increase of the magnetic field strength, P_0 seldom changes, but P_{50} gradually increases. Then A_3 is calculated according to the relationship between P_0 and P_{50}, and so does the magnetic field based on the relationship between A_3 and θ. The error between the calculated magnetic field and the magnetic field given by the simulation is less than 4.5%.

TABLE I
INVERSELY CALCULATED MAGNETIC FIELDS

Magnetic field (mT)	P_0	P_{50}	$A_3 = P_{50}/P_0$	Calculated magnetic field (mT)	Relative error
10	0.09618	0.000461	0.004792	10.4	4.40%
200	0.09618	0.008705	0.09051	197.1	1.44%
500	0.09618	0.02158	0.2243	490.9	1.83%
1000	0.09619	0.04210	0.4377	977.1	2.29%
1500	0.09619	0.06062	0.6302	1450.8	3.28%

3) Influence of Temperature Interference

The increase in temperature will lead to a decrease in the Verdet constant, and from (3) and (4), this will lead to a decrease in the Faraday rotation angle caused by the magnetic field, and so the variation of the output light intensity decreases. For TSAG crystal, the temperature changes from 25°C to 105°C, its Verdet constant decreases by about 23.9%. Without correction, this will lead to larger errors in the magnetic field measurement, making the measured results smaller [22], [23].

Table II shows the inversely calculated temperature and magnetic field according to the ratio. It can be found that the maximum relative error of the calculated temperature is 3.83%, which appears when the temperature is 45°C and the magnetic field is 10 mT. While the deviation of the inversely calculated magnetic field reaches the maximum value of 0.58%, when the temperature is 45°C and the magnetic field is 1000 mT. Under the same temperature and magnetic field, the error of temperature is about 4 times larger than that of magnetic field. When the magnetic field is 100 mT and 1000 mT, the calculation error is approximately equal, and the error gradually decreases with the increase of temperature. From the measurement results in Section III-A, the change rate of the ratio of the Verdet constants of TSAG to TGG crystals with temperature is less than 0.002 K^{-1}, meaning the ratio varies little with temperature. Therefore, when calculating the temperature according to the ratios of the Verdet constants, the temperature is very sensitive to the ratio of the Verdet constant. A slight deviation in the ratio calculated according to the light intensities of the two probes will lead to a deviation in the temperature calculation results. The deviation of the temperature calculation results in Table II is thus greater than 1%. However, the change rate of the Verdet constant of TSAG and TGG crystals with temperature is less than 0.26 rad/(T·m·K), meaning the sensitivity to temperature error is very low, so the error of the temperature calculation result has little effect on the calculation of the Verdet constant. The error of the final magnetic field calculation result is less than 0.58%, which shows the reliability of the temperature compensation method.

4) Influence of Vibration and Temperature Combined Interference

When considering the interference of vibration and temperature at the same time, since the temperature only affects the Verdet constant, and it can be seen from (1) and (9) the influence of temperature on the output light intensity is equivalent to the variation of the magnetic field. Therefore, when the influence of vibration and temperature interference are both considered, the waveform of the output light intensity is similar to the waveform when merely vibration interference is present. Due to length limitations, the waveforms of the output light intensity are not shown here.

Figure 8 shows the relative error of the inversely calculated magnetic field from the two-probe ratio at different temperatures and magnetic fields. We can see that when the magnetic field is low, because of the vibration amplitude given in the simulation, the light intensity fluctuation caused by the vibration is much larger than that caused by the alternative magnetic field, so the amplitudes of the 50 Hz, 150 Hz, 250 Hz and 350 Hz components are very low. While the truncation error and cumulative error in the numerical calculation are relatively large [25], resulting in a large relative error in the calculated two-probe ratio and temperature. Hence the relative error of the magnetic field calculation is a little large, but the absolute error does not exceed 1 mT. When the amplitude of the magnetic field is large, according to the aforementioned analysis of the influence of vibration and temperature, although the error of temperature calculation from the ratio of the

TABLE II
INVERSELY CALCULATED TEMPERATURE AND MAGNETIC FIELD UNDER DIFFERENT CONDITIONS

Given magnetic field	Give temperature (°C)	25	45	65	85	105
10 mT	Calculated temperature (°C)	25.26	43.28	65.31	85.19	102.51
	Calculated magnetic field (mT)	10.02	9.90	10.00	9.99	9.97
	Magnetic field error	0.20%	1.00%	0.00%	0.10%	0.30%
100 mT	Calculated temperature (°C)	25.59	43.88	66.22	86.36	105.24
	Calculated magnetic field (mT)	100.56	99.44	100.34	100.21	100.04
	Magnetic field error	0.56%	0.56%	0.34%	0.21%	0.04%
1000 mT	Calculated temperature (°C)	25.59	43.86	66.19	86.32	104.63
	Calculated magnetic field (mT)	1005.32	994.14	1003.16	1001.79	999.75
	Magnetic field error	0.53%	0.58%	0.32%	0.18%	0.03%

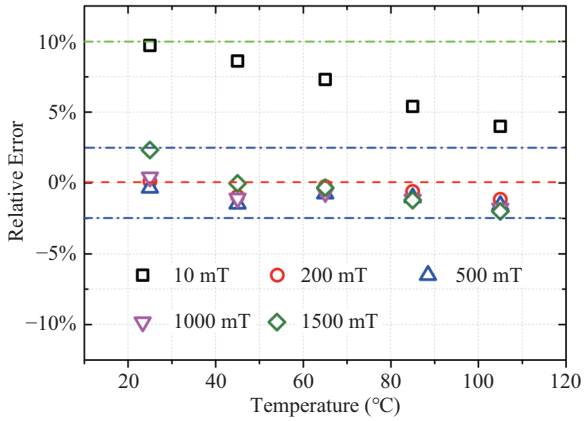

Fig. 8. Relative error of inversely calculated magnetic field at different temperatures and different magnetic fields.

two-probes is large, the error of the final magnetic field calculation result is about 2%. This error is mainly caused by the calculation method for eliminating the interference of vibration. These prove the interference suppression method is effective. However, eliminating the influence of numerical calculation errors on the magnetic field measurement needs to be further improved.

C. Sensitivity Analysis

From the above, the magnetic field sensitivity is related to the light intensity resolution. When 16-bit AD device with the voltage range of 0–10 V is adopted, the light intensity resolutions of the photoelectric detector are 11.22 nW and 1.122 nW on the gain of 20 dB and 40 dB, respectively. Then the sensitivity of the sensor can be obtained by calculating the relationship between the magnetic field change value and the 50 Hz integer multiple component of the output light intensity under different magnetic fields, as shown in Fig. 9. The larger the magnetic field, the lower the sensitivity of the magnetic field, but the deterioration is slight. The greater the gain, the higher the magnetic field sensitivity. When the gain of the photoelectric detector is 20 dB, the magnetic field sensitivity can approximately reach 0.8 mT; when the photoelectric detector selects a gain of 40 dB, the sensitivity can reach 0.1 mT. Both of them can achieve highly sensitive measurement of magnetic field.

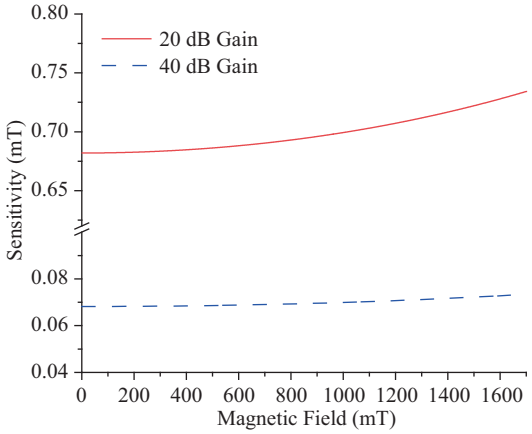

Fig. 9. Sensor sensitivity in the measurement range.

IV. Experimental Results and Analysis

A. Magnetic Field Measurement Test

The test platform is as shown in Fig. 10(a), which consists of a light source, a solenoid, the sensor, a high-precision AC power supply, a photoelectric detector, a 16-bit AD device and a vibration platform. The frequency of the vibration platform is 100 Hz, the fundamental frequency of the transformer, and the amplitude is simply divided into low amplitude and high amplitude. The sensor probe is placed in the center of the solenoid, and by adjusting the output of the high-precision AC power supply, the solenoid can generate an AC magnetic field of about 0–100 mT. For reference, the magnetic field is measured by a high-precision Tesla meter with a range of 0–3 T, a resolution of 0.01 mT, and an accuracy of 0.5%. With the help of the Tesla meter, we can adjust the amplitude of the magnetic field generated by the solenoid to ensure its deviation from the given value does not exceed 0.1 mT before each test of the sensor.

To better illustrate the anti-interference performance of the sensor in the subsequent interference test, the stability of the sensor is first tested in a non-interference environment. When an AC magnetic field of 24.7 mT is applied, the time and frequency domain output voltage waveform of the sensor is as shown in Fig. 10(b). We can see that the output voltage of the photoelectric detector mainly alternatively changes at a period of about 20 ms, and there are some high frequency noises from the power fluctuation of the light source or the ground noise of the photoelectric detector. But since the frequency of the noises is of thousands of hertz, and much higher than those of AC magnetic field and vibration, the high frequency noises have no influence on measurement. Due to the larger amplitude of the DC component, it is omitted from the frequency domain figure (the same for the following frequency domain waveform). We can see that there is only an obvious 50 Hz component, which is consistent with the previous analysis.

The developed sensor is used to measure the same magnetic field 10 times, and the interval between each measurement is one hour. The results are shown in Fig. 10(c), which shows that the fluctuation of the measurement results of the sensor is small, and the relative error of measurements is mostly less than 0.1%, and even the maximum one does not exceed 0.25%, indicating that the sensor has good measurement stability. Besides, the sensor and the solenoid have been impregnated into transformer oil to test whether transformer oil will affect the measurement performance of the sensor, as exhibited in Fig. 10(d). The measurement error between in transformer oil and air is merely 0.09 mT, meaning transformer oil has no influence on the measurement performance of the sensor.

B. Vibration Interference Test

When considering the vibration interference, the vibration platform is put into operation, and the optical fiber between the light source and the sensing probe is fixed onto the vibration platform. But since the light carrying the magnetic

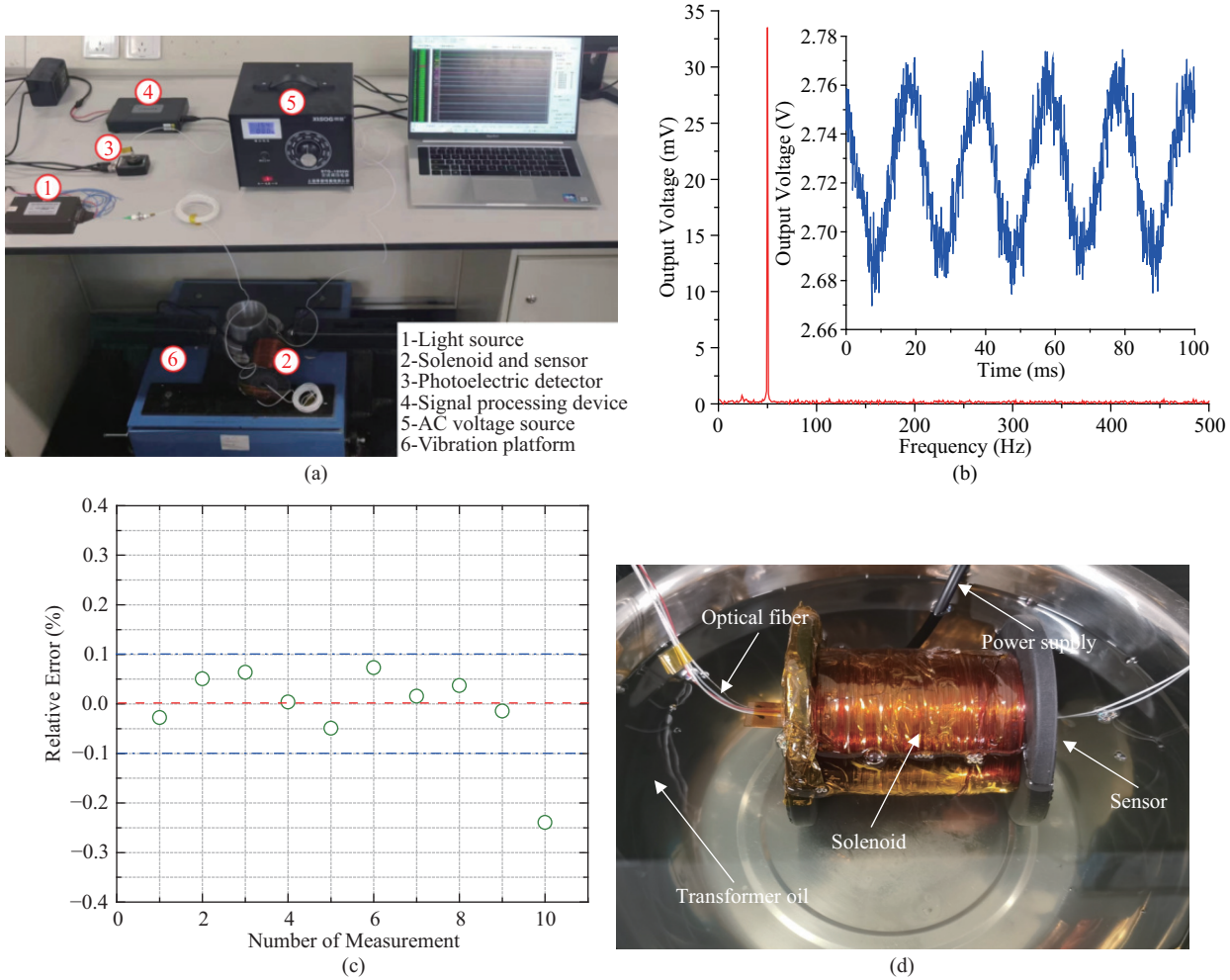

Fig. 10. Output signal of sensor without any interference. (a) Profile of the sensor performance test system. (b) Frequency and time domain waveform. (c) Relative error of multiple measurements. (d) Measurement in transformer oil.

field information has passed through the analyzer, no matter how vibration disturbs the optical fiber, its light intensity will not change [10], [19], so the optical fiber from the probe to the photoelectric detector does not need to be fixed on the vibration platform, as shown in Fig. 10(a).

First of all, no magnetic field is applied to the sensor, and only vibration is applied, the frequency domain output voltage waveform of the sensor is presented in Fig. 11(a). It can be seen that there are only the components at 100 Hz and 200 Hz, consistent with the theoretical analysis. The 200 Hz component can be originated from the interference of the vibration platform itself, or from the high-order component of the 100 Hz vibration interference [18], [19]. But from the previous analysis, it only influences the cross components at 150 Hz, 250 Hz and etc., so it will not affect the magnetic field measurement.

Then the MFS is applied with both vibration and magnetic field. The measurement results are shown in Fig. 11(b). With the proposed vibration interference suppression method, the measurement error caused by vibration interference is less than 1.13%, which verifies the effectiveness of the vibration interference suppression method.

C. Temperature Interference Test

The two probes are placed inside the solenoid at the same time, and then placed together in a drying oven, which can adjust the environmental temperature of the sensor and solenoid from 20°C to 140°C with an accuracy of 1°C. When the amplitude of the 50 Hz AC magnetic field is set as 32.5 mT, Fig. 12 compares the measurement error between the direct measurement of one probe and by the temperature interference compensation with the two-probe structure in the range of 25–95°C [26]. The measurement error increases with the increase of temperature before temperature compensation is performed, reaching 23.28% at 95°C. After temperature compensation, the maximum error is only 2.83%, which is reduced by about 10 times. This verifies the effectiveness of the temperature compensation method.

D. Vibration and Temperature Combined Interference Test

In the combined interference test, the two probes, solenoid, and vibration platform in Fig. 10(a) are placed together into the previously mentioned drying oven. When a 50 Hz AC magnetic field of 32.5 mT is generated and remains unchanged, Fig. 13 shows the comparison results of measurement errors under the combined interference of vibration and temperature.

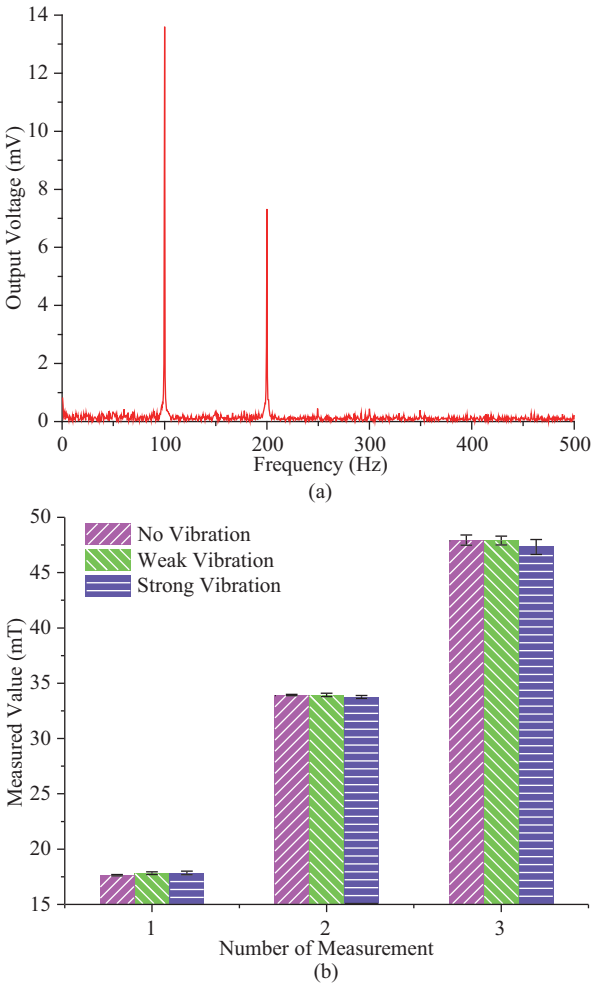

Fig. 11. Measurement results under different vibrations and magnetic fields. (a) Frequency domain output voltage under merely vibration interference. (b) Measurement results under vibrations and magnetic fields.

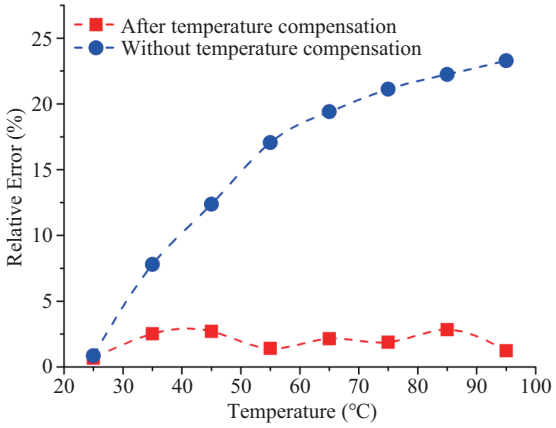

Fig. 12. Measurement error of magnetic field at different temperatures.

We can see that if the interference of temperature and vibration is not suppressed, the magnetic field measurement error can reach up to 80.56%. After the interference of vibration and temperature is suppressed by the characteristic frequency separation method and the two-probe structure, the relative error is less than 2.63%. It validates that the vibration separation and temperature compensation methods can effectively improve the accuracy of magnetic field measurement under the condition of vibration and temperature combined interference.

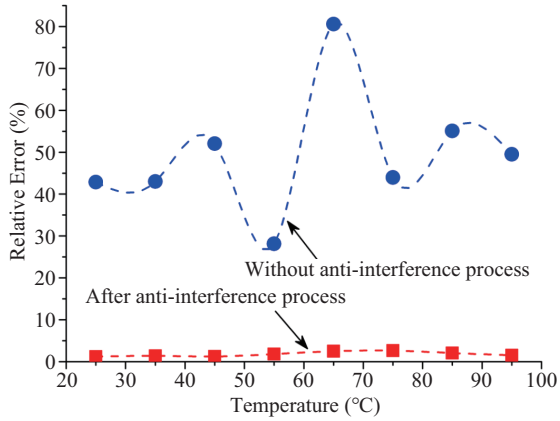

Fig. 13. Measurement error of magnetic field under vibration and temperature combined interference.

E. Sensor Performance Calibration

Since it is difficult to generate a strong AC magnetic field in the range of 200 mT–1.5 T, this paper can only calibrate the accuracy and sensitivity of the sensor measurement in the range of 10–100 mT based on the test platform illustrated in Fig. 10(a). Fig. 14 shows the calibration of the measurement accuracy and sensitivity of the sensor. The gain of the photoelectric detector is set to 20 dB during the measurement. It can be clearly seen that in the range of 10–100 mT, the linearity of the sensor is better than 0.9999, the deviation is less than 1.83%, and the resolution is 1 mT, which verifies that the developed MFS has excellent accuracy and sensitivity.

According to the previous principle analysis and simulation results, the magnetic field mainly affects the output light intensity by changing the Faraday rotation angle of the MOC. When the magnetic field is strong, the 50 Hz component of the output light intensity is large, and the influence of the error from the numerical calculation in the signal processing process is small. Hence the main factor that affects the accuracy of the sensor to measure the strong magnetic field is the degree of linearity between the Faraday rotation angle and the magnetic field strength [27]. The Faraday rotation angle of the MOC under DC magnetic field is proportional to the magnetic field strength, so the linearity between the strength of the DC magnetic field and the measured value under the condition of no vibration and temperature interference can be used to indirectly calibrate the accuracy of the sensor, for measuring strong AC magnetic field [27].

The strong DC magnetic field is generated by a cylindrical permanent magnet and the maximum value is about 1.8 T. The sensor probe is placed parallel to the axis of the permanent magnet and the amplitude of the DC magnetic field is adjusted by changing their distance. The comparison between the DC magnetic field strength and the measured value of the sensor is shown in Fig. 14(c). The fitting slope between the measured value and the given value is 0.9965, and the accuracy of fit is 0.9988, indicating that the Faraday rotation angle has a good

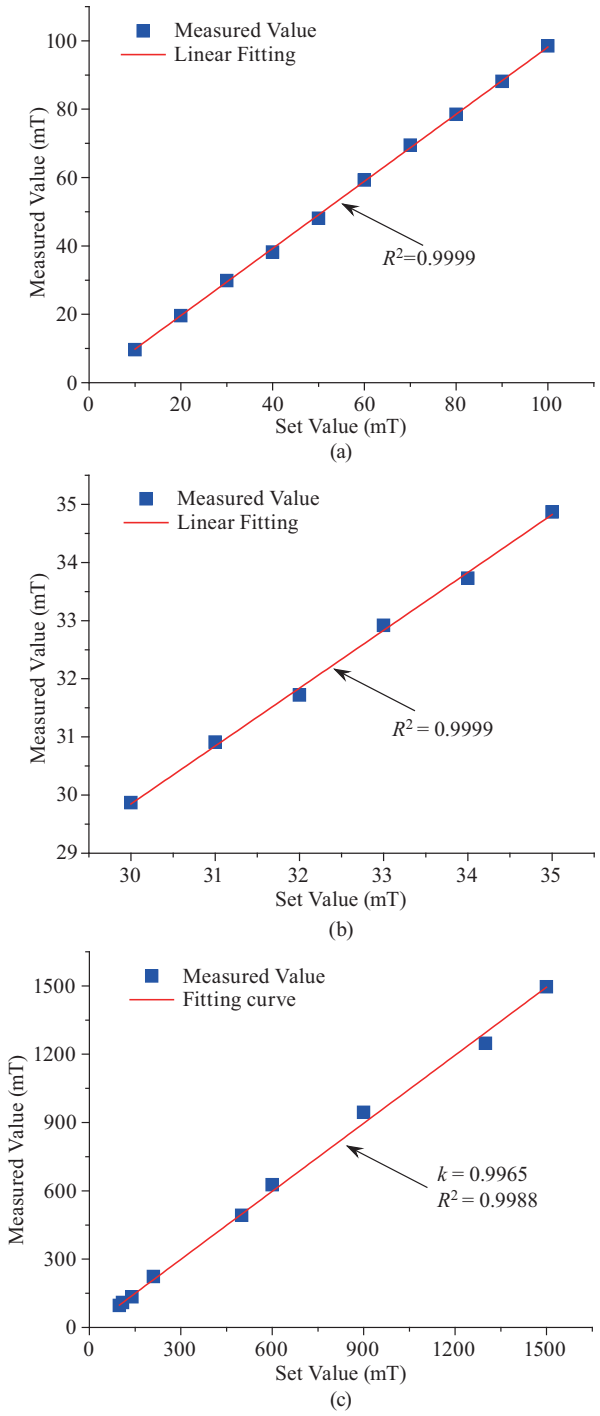

Fig. 14. Accuracy and sensitivity calibration of the sensor. (a) Accuracy. (b) Sensitivity. (c) Measurement linearity of DC magnetic field in a wide range.

linear relationship with the magnetic field strength under a wide range of magnetic fields. That is, the sensor has good accuracy and sensitivity in the range of 10 mT–1.5 T. The result obtained in this paper is compared with literature results, as shown in Table III. From Table III, it is observed that the proposed sensor has good sensitivity and operating range, which are better than the previously reported sensors.

V. Conclusion

Based on the Faraday effect of TSAG and TGG MOCs, an MFS suitable for the monitoring of leakage magnetic field inside power transformers is proposed. By selecting an appropriate length of the MOC, the probe size can be small, while the sensor is with a wide range and high sensitivity. The performance calibration test of the sensor shows that the measurement range is 10 mT–1.5 T, and the sensitivity is better than 1 mT. However, the performance under strong AC magnetic field needs to be further verified by experiments, and the further miniaturization of the sensor also needs to be studied. Vibration and temperature are the two key factors affecting the measurement accuracy of the sensor, and the error can even reach 80.56%. The characteristic frequency analysis method and the two-probe structure are used to suppress the vibration interference and compensate the temperature interference. The anti-interference test results show that the measurement error of the sensor is less than 2.63% after interference processing. However, the error caused by the numerical calculation can be further improved, and it is expected to realize the simultaneous measurement of vibration, temperature and magnetic field three parameters through signal processing method.

TABLE III
Key Parameters of Some Kinds of Optical Magnetic Field Sensors

References	Techniques	Measurement Range	Sensitivity
[13]	Faraday effect	−6 T∼6 T	10 mT
[14]	Kerr and Faraday effect	0∼200 mT	0.224 mT
[28]	Faraday effect	0.02∼3.2 T	4.51 mT
This paper	Faraday effect	10 mT∼1.5 T	1 mT

Appendix

A. Leakage Magnetic Field Distribution Simulation

The leakage magnetic field distribution in a three-winding 110 kV power transformer, whose parameters are listed in Table AI, is simulated by the finite element method.

TABLE AI
Parameters of the 110 kV Power Transformer

Quantity	Vaulue
Capacity	250 kVA
Voltage	110/35/10.5 kV
Winding height (coil only)	629 mm
Winding height (overall)	825 mm
High voltage (HV) winding radius	481.5–558.0 mm
Medium voltage (MV) winding radius	388.5–449.5 mm
Low voltage (LV) winding radius	315.0–369.5 mm
Number of HV/MV/LV winding turn	623/198/103

For briefness, just one-phase winding is taken for analysis, and a two-dimensional axisymmetric model of the transformer is established, as shown in Fig. A1(a). During the simulation of normal operation, the rated current is applied to the winding, and the leakage magnetic field distribution is shown in Fig. A2.

We can see that the maximum leakage magnetic field can reach 371 mT and it appears in the oil gap between the HV and the MV winding. Whereas the minimum one appears in that between the iron core and the LV winding, which is 3 mT. As regards the local magnetic field distribution near the winding, its amplitude varies between 4 mT and 371 mT.

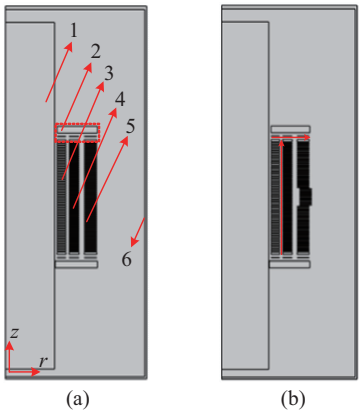

Fig. A1. Simulation model of transformer. 1-iron core;2-insulation of the winding end; 3-LV winding; 4-MV winding; 5-HV winding; 6-tank wall. (a) Normal. (b) Radial deformation.

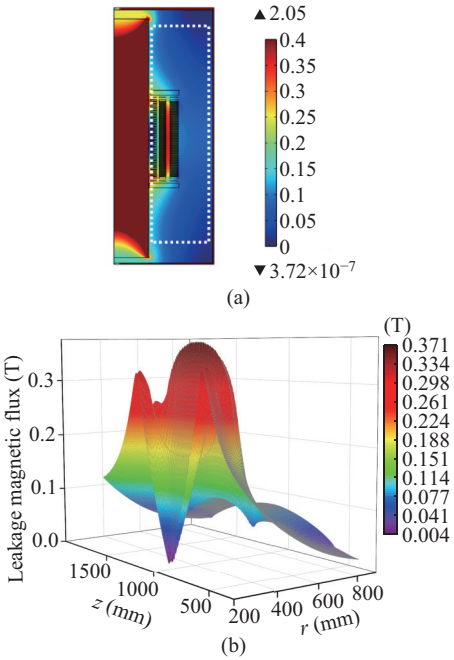

Fig. A2. Leakage magnetic field distribution under normal operation. (a) Overall view. (b) Local distribution near the winding.

For winding deformation simulation, we consider both radial deformation and axial deformation. The deformation degree is set as 20% of the winding size (radius or height) in the deformation direction, and for instance, the model of radial deformation on HV winding is illustrated in Fig. A1(b). Fig. A3 compares the local leakage magnetic field variation of different kinds of winding deformation at different positions. The leakage magnetic field changes obviously by winding deformations in different directions and at different positions, and the variation can be as high as 43.6 mT. The largest variation generally occurs near the defective coil, and the farther away from it, the variation becomes smaller.

For inter-turn short circuit simulation, the short-circuit current is applied to the defective coil, and it is set as 20 times of the normal operation current. Fig. A4 displays the variation of leakage magnetic field under the condition of inter-turn

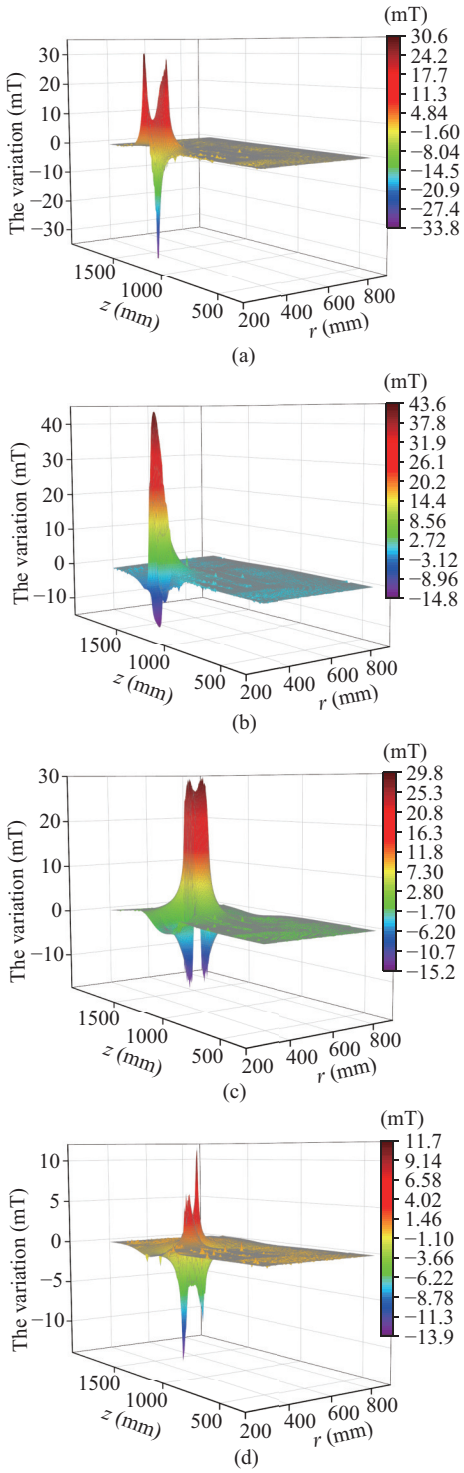

Fig. A3. Leakage magnetic field variation of winding deformations. (a) Radial deformation of LV winding. (b) Axial deformation of LV winding. (c) Radial deformation of HV winding. (d) Axial deformation of HV winding.

short circuit of 5% disc coils. When the inter-turn short circuit occurs in the LV winding, the maximum variation of leakage magnetic field can be up to 1.1 T, but if the inter-turn short circuit occurs in the HV winding, it is just 652 mT.

B. Detection Method of Leakage Magnetic Field

Since the leakage magnetic field distribution is different

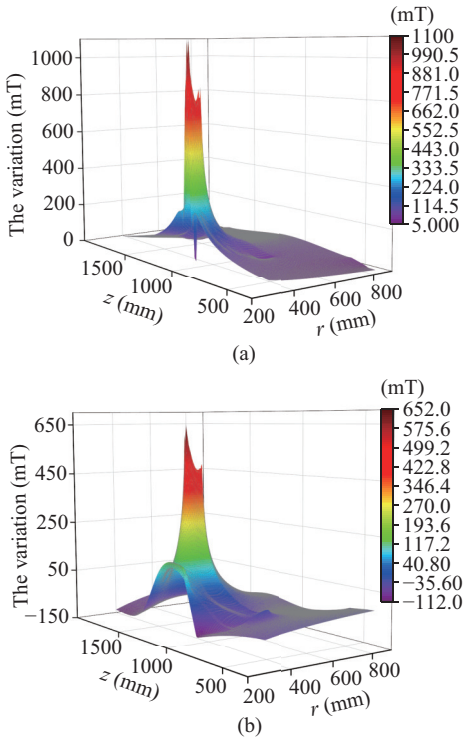

Fig. A4. Leakage magnetic field variation of inter-turn short circuits. (a) Middle part of LV winding. (b) Upper part of HV winding.

with different kinds and degrees of winding defects at different positions, it is difficult to monitor winding defects with merely one sensor. With the simulation results of different kinds and degrees of winding defects at different positions, we find that when winding deformation occurs at the upper part of the winding, the leakage magnetic field along the internal insulation of the winding end changes significantly, up to 17 mT. However, when winding deformation takes place in the middle of the winding, the leakage magnetic field on that path only changes 0.2 mT. In the case of inter-turn short circuit, even if it occurs in the middle of the winding, the variation of leakage magnetic field can be larger than 100 mT. Therefore, to realize effective monitoring of winding deformation and inter-turn short circuit, MFS need to be installed near the winding end insulation and in the middle outside the LV winding. A schematic diagram of the installation positions of a 5-sensor detection method is as shown in Fig. A5. Because the relative permeability of the materials used in the manufactured sensor can be seen as equal to those of the insulation materials around the installation position, the installation will not affect the distribution of transformer leakage magnetic field.

Then the winding defects can be distinguished from the variation of leakage magnetic field of the five sensors. For winding deformation, variations of leakage magnetic field of defects at different positions are listed in Table AII. The output of each sensor is different for different kinds of winding deformation at different positions, so we encode the outputs of the five sensors for easy and fast recognition. The coding rule is: if the variation of leakage magnetic field is larger than 4 mT, it is assigned a value of 2, and if the variation is between 0.3 mT and 4 mT, it is assigned a value of 1, otherwise if the

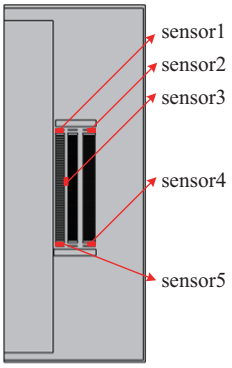

Fig. A5. Schematic diagram of sensor installation for 5-sensor detection.

TABLE AII
LEAKAGE MAGNETIC FIELD VARIATION OF WINDING DEFORMATION

Defect[a]	Sensor 1[b]	Sensor 2	Sensor 3	Sensor 4	Sensor 5
LUR	12.22	−0.23	0.28	0.02	0.05
LMR	0.21	0.06	−5	0.05	0.2
LUA	−4.33	−0.22	0.39	0.14	0.28
LMA	−0.74	−0.33	9.14	0.28	0.64
MUR	4.75	−0.92	0.52	0.07	0.14
MMR	0.52	0.18	−8.82	0.17	0.52
MUA	1.49	−0.29	0.11	0.06	0.12
MMA	−0.27	−0.15	−3.1	0.13	0.25
HUR	1.45	6.25	0.41	0.18	0.36
HMR	0.94	0.51	−2.01	0.5	0.96
HUA	−0.73	3.12	0.04	−0.05	−0.11
HMA	0.13	0.1	0.19	−0.1	−0.15

[a]The first word L, M, and H refer to LV, MV and HV winding. The second word U and M refer to upper and medium part. And the third word R and A refer to radial and axial deformation, respectively.
[b]The unit for output of sensor 1 to 5 is mT.

TABLE AIII
CODE OF DIFFERENT WINDING DEFORMATION

Defect	Sensor 1	Sensor 2	Sensor 3	Sensor 4	Sensor 5	Decimalism
LUR	2	0	0	0	0	162
LMR	0	0	2	0	0	18
LUA	2	0	1	0	0	171
LMA	1	1	2	0	1	127
MUR	2	1	1	0	0	198
MMR	1	0	2	0	1	100
MUA	1	0	0	0	0	81
MMA	0	0	1	0	0	9
HUR	1	2	1	0	1	145
HMR	1	1	1	1	1	121
HUA	1	1	0	0	0	108
HMA	0	0	0	0	0	0

variation is smaller than 0.3 mT, it is assigned zero. The code corresponding to Table AII is exhibited in Table AIII. The code is transferred to a decimal number, as listed on the last column. We can see that the code and number is obviously different for different winding deformations at various positions.

As regards the inter-turn short circuit defects, variations of leakage magnetic field of defects at different positions are shown in Table AIV, and the variations are much higher than those in Table AII. Then we similarly encode the outputs of the five sensors with the two critical values of leakage magnetic field variations separately setting as 120 mT and 0 mT. The code corresponding to Table AIV is exhibited in Table AV. A unique decimal number is generated corresponding to inter-

TABLE AIV
LEAKAGE MAGNETIC FIELD VARIATION OF INTER-TURN SHORT CIRCUITS

Defect[a]	Sensor 1[b]	Sensor 2	Sensor 3	Sensor 4	Sensor 5
LU	465.6	126.83	60.82	31.62	60.6
LM	101.88	52.66	699.24	53.49	104.91
MU	102.31	149.03	48.26	29.38	56.31
MM	111.74	60.31	38.31	61.31	114.78
HU	−11.78	165.83	22.9	−28.54	−77.87
HM	−101.23	−28.3	81.72	−26.36	−110.95

[a]The first word L, M, and H refer to LV, MV and HV winding. The second word U and M refer to upper and medium part, respectively.
[b]The unit for output of sensor 1 to 5 is mT.

TABLE AV
CODE OF INTER-TURN SHORT CIRCUITS

Defect	Sensor 1	Sensor 2	Sensor 3	Sensor 4	Sensor 5	Decimalism
LU	2	2	1	1	1	229
LM	1	1	2	1	1	130
LB[a]	1	1	1	2	2	125
MU	1	2	1	1	1	148
MM	1	1	1	1	1	121
MB	1	1	1	2	1	124
HU	0	2	1	0	0	63
HM	0	0	1	0	0	9
HB	0	0	1	2	0	15

[a]The second word B refers to bottom part.

turn short circuit defects at different positions. Though some decimal numbers are the same as those of winding deformation defects, the maximum change of leakage magnetic field caused by inter-turn short circuits can reach 466 mT, which is much larger than that of 12 mT by winding deformation, so it could be easily distinguished.

Therefore, an MFS with large range of 60 mT to 1.1 T and high sensitivity better than 1 mT can help realize monitoring and diagnosis of internal transformer defects of winding deformation and inter-turn short circuits.

REFERENCES

[1] K. X. Hong, L. Wang, and S. Xu, "A variational mode decomposition approach for degradation assessment of power transformer windings," *IEEE Transactions on Instrumentation and Measurement*, vol. 68, no. 4, pp. 1221–1229, Apr. 2019.

[2] F. Haghjoo and H. Mohammadi, "Planar sensors for online detection and region identification of turn-to-turn faults in transformers," *IEEE Sensors Journal*, vol. 17, no. 17, pp. 5450–5459, Sep. 2017.

[3] A. P. Iyer, A. Goj, and O. K. Ahmed, "Performance of depressurization devices to dynamic loads generated by arcing in liquid filled transformers," presented at *ASME 2018 Pressure Vessels and Piping Conference*, Prague, Czech Republic, Jul. 15–20, 2018.

[4] W. L. Liao, D. C. Yang, Y. S. Wang, and X. Ren, "Fault diagnosis of power transformers using graph convolutional network," *CSEE Journal of Power and Energy Systems*, vol. 7. no 2, pp. 241–249, Mar. 2021.

[5] M. Mostafaei, J. Faiz, P. A. Venikar, and M. S. Ballal, "Turn-to-turn fault monitoring methods in electrical power transformers—state of the art," *International Transactions on Electrical Energy Systems*, vol. 28, no. 12, pp. e2644. Dec. 2018.

[6] Y. Zhao, W. J. Chen, M. K. Jin, T. Wen, J. Y. Xue, Q. G. Zhang, and M. Chen, "Short-circuit electromagnetic force distribution characteristics in transformer winding transposition structures," *IEEE Transactions on Magnetics*, vol. 56, no. 12, pp. 8400708, Dec. 2020.

[7] V. Schukar, E. Köppe, D. Hofmann, A. Westphal, M. Sahre, X. Gong, M. Bartholmai, and U. Beck, "Magnetic field detection with an advanced FBG-based sensor device," in *Proceedings of the 30th Anniversary Eurosensors Conference*, 2016, pp. 1270–1274.

[8] E. Kendir and Ş. Yaltkaya, "Variations of magnetic field measurement with an extrinsic Fabry-Perot interferometer by double-beam technique," *Measurement*, vol. 151, pp. 107217, Feb. 2019.

[9] X. X. Feng, Y. Jiang, and H. Zhang, "A mechanical amplifier based high-finesse fiber-optic Fabry–Perot interferometric sensor for the measurement of static magnetic field," *Measurement Science and Technology*, vol. 32, no. 12, pp. 125106, Dec. 2021.

[10] A. Dufour, L. Bsawmaii, D. Jamon, E. Marin, S. Neveu, S. Reynaud, S. Girard, and F. Royer, "All-fiber magneto-optical effect using nanoparticles doped sol-gel thin film deposited within microstructured fibers," *Journal of Lightwave Technology*, vol. 39, no. 17, pp. 5604–5610, Sep. 2021.

[11] S. Y. Yin, Z. Z. Zhang, Y. Li, H. Wang, L. Liu, T. J. Zhou, and S. F. Wang, "Faraday angle and accuracy measurement of magneto-optic current transmission based on new telluride glass," *IEEE Photonics Journal*, vol. 14, no. 5, pp. 6852706, Oct. 2022.

[12] J. X. Li, T. Wen, X. Fan, B. Y. Chen, M. K. Jin, Y. Zhao, Q. G. Zhang, and W. J. Chen, "Research on the influence of temperature on the sensing function of faraday effect optical magnetic field sensor," *Measurement Science and Technology*, vol. 33, no. 9, pp. 095102, Sep. 2022.

[13] J. X. Li, Y. Zhao, T. Wen, X. Fan, W. J. Chen, Q. G. Zhang, and Z. Y. Wu, "An optical fiber magnetic field sensor based on Faraday effect for transformer leakage magnetic field measurement," in *Proceedings of 2021 IEEE Electrical Insulation Conference*, 2021, pp. 137–140.

[14] A. A. D. da Silva, H. P. Alves, F. C. Marcolino, J. F. do Nascimento, and J. F. Martins-Filho, "Computational modeling of optical fiber-based magnetic field sensors using the faraday and Kerr magnetooptic effects," *IEEE Transactions on Magnetics*, vol. 56, no. 9, pp. 4001109, Sep. 2020.

[15] C. Pan, C. J. Wang, and H. Su, "Excitation current and vibration characteristics of DC biased transformer," *CSEE Journal of Power and Energy Systems*, vol. 7, no. 3, pp. 604–613, May 2021.

[16] X. Y. Jia, M. Lin, S. W. Su, Q. W. Wang, and J. Yang, "Numerical study on temperature rise and mechanical properties of winding in oil-immersed transformer," *Energy*, vol. 239, pp. 121788, Jan. 2022.

[17] X. C. Wang, J. T. Hu, F. Wang, Y. Q. Yong, Y. X. Zhang, M. Xue, X. P. Zhang, and S. L. Pan, "Multi-vibration detection by probe pulses with ergodic SOPs in a POTDR system," *Optics Express*, vol. 26, no. 22, pp. 28349–28362, Oct. 2018.

[18] F. Wang, Y. Pan, M. Zhang, C. Q. Cao, and X. P. Zhang, "Detection of two identical frequency vibrations by phase discrimination in polarization-OTDR," *Optics Communications*, vol. 389, pp. 247–252, Apr. 2017.

[19] X. C. Wang, X. P. Zhang, F. Wang, M. M. Chen, and C. L. Li, "Application of frequency spectrum analysis in measuring multi-vibrations by using POTDR," in *Proceedings of SPIE 8198, 2011 International Conference on Optical Instruments and Technology: Optoelectronic Devices and Integration*, 2011, pp. 819808.

[20] M. Y. Zhao and G. Xu, "Feature extraction of power transformer vibration signals based on empirical wavelet transform and multiscale entropy," *IET Science, Measurement & Technology*, vol. 12, no. 1, pp. 63–71, Jan. 2018.

[21] O. Slezák, R. Yasuhara, A. Lucianetti, and T. Mocek, "Temperature-wavelength dependence of terbium gallium garnet ceramics verdet constant," *Optical Materials Express*, vol. 6, no. 11, pp. 3683–3691, Nov. 2016.

[22] Y. H. Huang, L. Xia, F. B. Pang, Y. B. Yuan, and J. F. Ji, "Self-compensative fiber optic current sensor," *Journal of Lightwave Technology*, vol. 39, no. 7, pp. 2187–2193, Apr. 2020.

[23] I. L. Snetkov, R. Yasuhara, A. V. Starobor, E. A. Mironov, and O. V. Palashov, "Thermo-optical and magneto-optical characteristics of terbium scandium aluminum garnet crystals," *IEEE Journal of Quantum Electronics*, vol. 51, no. 7, pp. 7000307, Jul. 2015.

[24] B. Peng, X. Z. Wei, B. Deng, H. W. Chen, Z. Liu, and X. Li, "A sinusoidal frequency modulation Fourier transform for radar-based vehicle vibration estimation," *IEEE Transactions on Instrumentation and Measurement*, vol. 63, no. 9, pp. 2188–2199, Sep. 2014.

[25] E. M. G. Diaz, G. S. Wei, and L. Cui, "CFD analysis of an 800 kV HVDC transformer using rapeseed oil as the cooling fluid," *CSEE Journal of Power and Energy Systems*, vol. 8, no. 5, pp. 1508–1518, Sep. 2022.

[26] T. Qian, Q. L. Wei, Z. Y. Yu, W. H. Tang, and Q. H. Wu, "Multi-parametric sensitivity analysis of improved transformer thermal models considering nonlinear effect of oil time constant," *CSEE Journal of Power and Energy Systems*, vol. 9, no. 5, pp. 1950–1958, Sep. 2023.

[27] K. Okubo and O. Kamada, "Magnetic field optical sensors using (TbY)IG crystals with stripe magnetic domain structure," *IEEE Transactions on Magnetics*, vol. 41, no. 10, pp. 3640–3642, Oct. 2005.

[28] L. Sun, S. Jiang, and J. R. Marciante, "All-fiber optical magnetic-field sensor based on Faraday rotation in highly terbium-doped fiber," *Optics Express*, vol. 18, no. 6, pp. 5407–5412, Mar. 2010.

Meng Huang received the B.Eng. (2011) and Ph.D. (2016) degree in Electrical Engineering from Tsinghua University. Now, he is a teacher at School of Electrical and Electronic Engineering, North China Electric Power University. His research activities are mainly in the field of oil-paper insulation, organic dielectrics, high voltage technology and space charge measurement.

Wei Zheng received the B.S. degree and M.S. degrees in Electrical Engineering from North China Electric Power University, Beijing, China, in 2019 and 2022, respectively. He is currently an Engineer with the State Grid Bishan Power Supply Company, Chongqing, China. His research interests include development of advanced sensing devices.

Tong Ji received the B.S. degree in Electrical Engineering from the Xi'an University of Architecture and Technology in 2016. He is currently pursuing the M.S. degree in Electrical Engineering at North China Electric Power University. His research interests include Fiber Bragg grating sensor for transformer on-line monitoring.

Mao Ji received the B.S. degree in Electrical Engineering from North China Electric Power University, in 2017. He is currently pursuing the Ph.D. degree in Electrical Engineering with North China Electric Power University. His research interests include development of advanced sensing devices and online monitoring of electrical equipment.

Tianjiao Pu received the B.S. degree from the Department of Electric Power Systems and Automation of Tianjin University in 1997 and has worked ever since at China Electric Power Research Institute. He is a Professorate Senior Engineer, the director of the Artificial Intelligence Application Research Department of China Electric Power Research Institute (CEPRI), a core member of the "Science and Technology Tackling Team of Energy-saving Economic Dispatching" in State Grid Corporation of China, a Fellow of IET, a senior member of IEEE, a senior member of CSEE, a CIGRE member, Secretary General of the AI Committee of CSEE, and a Deputy Editor-in-Chief of *IET Smart Grid*. He has been engaged in the research and management of power dispatching automation, smart grid simulation, active distribution network, artificial intelligence and other fields.

Bo Qi received the B.S. degree in Electrical Engineering, the M.S. degree in High Voltage and insulation, and the Ph.D. degree in High Voltage and insulation from North China Electric Power University (NCEPU), Beijing, China, in 2003, 2006, and 2010, respectively. He is currently an Associate Professor with the School of Electric and Electronic Engineering, NCEPU. His current research interests include condition monitoring of power apparatus, space charge measurement, electrical insulation, and materials.